Journal of Aerosol Science 65 (2013) 58–68

Contents lists available at ScienceDirect

Journal of Aerosol Science

journal homepage: www.elsevier.com/locate/jaerosci

Inhalation and deposition of carbon and glass composite fibre in the respiratory airway

Kiao Inthavong, Adrian P. Mouritz, Jingliang Dong, Ji Yuan Tu*

School of Aerospace, Mechanical and Manufacturing Engineering, RMIT University, PO Box 71, Bundoora Vic 3083, Australia

ARTICLE INFO

Article history:
Received 21 March 2013
Received in revised form
28 May 2013
Accepted 2 July 2013
Available online 16 July 2013

Keywords:
Composite fibre
Nasal deposition
Deposition patterns
Fibre drag
Realistic nasal model

ABSTRACT

This paper presents a comparative study into the inhalation by the human respiratory system of airborne carbon and glass fibres released from burning composite materials used in aircraft. Using experimental data on the release of fibres from composites produced from fires, carbon and glass fibres of varying lengths were evaluated for their likely deposition in the human respiratory airway during inhalation. An anatomical model of the respiratory system coupled with a computational fluid dynamics (CFD) model was used to analyse the fibre trajectories from the outside air, through the nostrils, and into the respiratory system (including the larynx, trachea and lungs). Deposition of carbon fibres were more influenced by their length than glass fibres, which is attributed to their lower density and smaller diameter. Local deposition fractions showed that all fibres either deposited mainly in the nasal cavity or penetrated through to the lungs.

1. Introduction

The superior physical and engineering properties of carbon fibre reinforced polymer matrix composites have seen these materials replacing traditional aluminium alloys in aircraft structures such as the fuselage and wings. Glass fibre composites are used extensively in aircraft cabins for their light-weight, good mechanical properties and low cost, and applications include overhead luggage containers and partitions. A concern with using carbon and glass reinforced composites in aircraft is the release of fibres into the smoke plume in the event of a post-crash fire. The polymer matrix of composites is flammable, and fibre fragments can be released as fine respirable particles once the matrix has decomposed. The release of fibres poses a potential health risk to passengers and crew as well as response teams attending aircraft crash sites. This has been confirmed through reported health problems that varied in severity from eye and skin irritations to severe breathing difficulties (Gandhi, et al., 1999; Tannen, 1993). With the rapid growth in the use of fibre reinforced composites in aircraft, there is a growing concern about the health hazards of exposure to airborne carbon and glass fibres released in a post-crash fire.

Airborne ultrafine fibrous particles present a further danger as such particles are highly respirable, thereby allowing entrance into the respiratory airway. Past studies of fibrous particles based on asbestos have revealed the deleterious health effects caused by deposition in the respiratory airway, leading to pleural disorders, mesothelioma or lung cancer after a long latency period. The levels of toxicity vary and is dependent on the fibre length and their biopersistence in the lungs (Lippman, 1990; Timbrell, 1982). The delayed and long-term health problems is of major concern and a better understanding

* Corresponding author. Tel.: +61 3 9925 6191; fax: +61 3 9925 6108.
E-mail address: jiyuan.tu@rmit.edu.au (J.Y. Tu).

0021-8502/$ - see front matter © 2013 Elsevier Ltd. All rights reserved.
http://dx.doi.org/10.1016/j.jaerosci.2013.07.003

of the deposition rates of fibrous particles may help plan for better preventative measures. Despite the potential dangers posed by inhalation of composite fibres, medical researchers, toxicologists, and the aviation industry have paid scant attention to the health effects of smoke generated by composite materials, including small fragments of airborne fibres (Mouritz, 2009).

Controlled exposure studies to airborne particles on human subjects have been performed by Cheng et al. (1996), albeit for non-toxic particles. For toxic particles the use of rodent subjects as human surrogates are used (Mossman et al., 2011), but often the dosage is instilled directly into the respiratory airway. Exposure chambers provide a more realistic exposure environment for natural inhalation, but determining the actual dosage is difficult (Jeon et al., 2012; O'Shaughnessy et al., 2003). Post-mortem examination of laboratory animals exposed to high concentrations of carbon or glass fibres has revealed no long-term toxicity, although there are short-term health problems such as laboured breathing (Hesterberg et al., 1993; Martin et al., 1989; Owen et al., 1986; Whitehead et al., 2003).

There are few studies that have investigated fibre deposition in the human airway. Using a cast chamber Gradoń and Podgórski (1992) studied the deposition of glass fibres (density $=2.2$ g/cm^3) with a diameter of 0.8 μm and aspect ratio $\beta=10$, 20 and 40, and they found that deposition was not influenced significantly by particle length, as is spherical particles of equivalent mass. Su and Cheng (2005) also investigated the deposition patterns in a cast nasal cavity of carbon fibres, monodisperse in diameter (3.66 μm), polydisperse in length, and density at 1.83 g/cm^3 at different constant flow rates. They found that impaction was the dominant deposition mechanism and most of the fibres exhibited high inertia and deposited in the anterior region of the nasal cavity (vestibule and nasal valve regions). Later Wang et al. (2008) integrated the influence of particle length, flow rate, and geometry of a nasal airway on fibre deposition and defined an effective aerodynamic diameter such that the deposition efficiencies of glass fibres were comparable with those of spherical particles. These studies present the nasal cavity cast separately, and have excluded the influences of the face (King Se et al., 2010), external environment, and also additional regions of the respiratory airway.

In this study, a computational anatomical model of the human respiratory system is coupled with a computational fluid dynamics (CFD) model to analyse and quantify the dosimetry of inhaled carbon and glass fibres within simulated smoke generated by burning composite materials. An empirically defined drag coefficient by which accounts for the random fibre orientation through the flow field has been determined (Tran-Cong et al., 2004). Applying this drag coefficient directly onto an equivalent Lagrangian particle provides an alternative approach to the established numerical technique applied by Asgharian and Anjilvel (1995) and Shanley and Ahmadi (2011) that integrates a force balance onto rigid body, thus allowing fibre rotation to be considered explicitly. This paper uses the former approach and extends the nasal cavity geometry model to include facial features, the external environment and to investigate the inhalation effects on the deposition and hence the dosimetry of carbon and glass fibre fragments.

2. Methods

2.1. Geometry model development

A computational fluid dynamics (CFD) model of the upper respiratory airway containing the nasal cavity, larynx, trachea and first bifurcation of the bronchial airway tree is developed from CT scans of individual regions of the human respiratory airway (Inthavong et al., 2009, 2010a, 2011). Each model of the respiratory airway is connected to form a contiguous path from the nostril inlets to the upper tracheal region. Artificial straight tubes that extend from the first lung bifurcation are created to allow sufficient flow recovery and assist in numerical convergence of the CFD solution. The respiratory airway is then added to a realistic human face, and is exposed to the external surroundings containing airborne carbon or glass fibres. A high quality mesh (minimum orthogonality >0.1) incoporating prism layers was applied to the bounding respiratory walls. A tetrahedral unstructured mesh filled the airway passage. The mesh was gradually expanded out minimising large changes in mesh size to resolve the fluid domain around the head. The final model is shown in Fig. 1, which consists of 7 million cells. Visualisation and generation of the mesh was possible on a workstation with 32 Gb Ram 4 Gb video card, and 8 processor cores. The simulations were performed on a High Performance Computing cluster with has 268 processor cores. Further details of the computational model is given in Inthavong et al. (2012).

2.2. Fluid flow modelling

The commercial CFD code, Ansys-Fluent v14.0, is used to predict the continuum air flow. The surrounding walls are set to atmospheric pressure while the flow field is initiated by a negative pressure difference induced at the bronchial airway bifurcation. This allows the flow field surrounding the face to be ambient ($u_i=0$ m/s) and only influenced by the inhaled air, which is set to a flow rate of 15 l/min (LPM). The external flow conditions can have an influence on the inhalability of the particles which include flow orientation, freestream velocity, and the upstream location of the particle origin to name a few. These conditions have been reported in separate studies by Anthony and Flynn (2006), Kennedy and Hinds (2002), and Inthavong et al. (2013), among others and is not investigated in this paper.

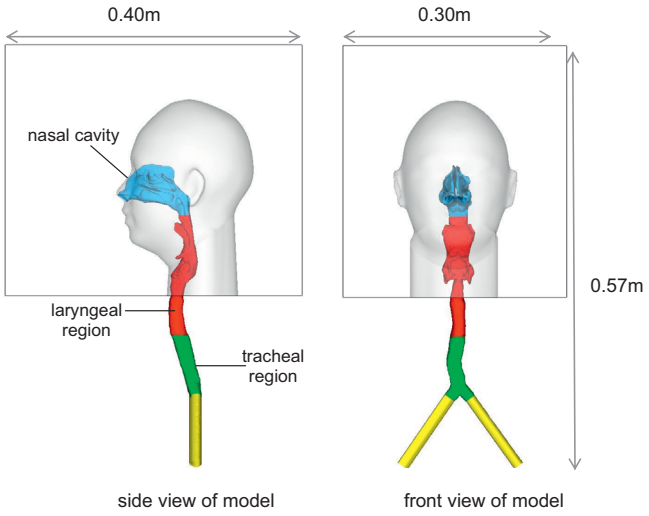

Fig. 1. Computational model of the respiratory airway connected to the outside air for exposure studies. The model is segmented into four regions. Blue: nasal cavity; red: laryngeal region; green: tracheal region; and yellow: artificial extensions.

The governing equations for the fluid flow are

Continuity equation:

$$\frac{\partial}{\partial x_i}(\rho_g u_i^g) = 0 \tag{1}$$

Momentum equation:

$$\rho_g u_i^g \frac{\partial u_i^g}{\partial x_j} = -\frac{\partial p_g}{\partial x_i} + \frac{\partial}{\partial x_j}\left[\mu_g \frac{\partial u_i^g}{\partial x_j}\right] \tag{2}$$

where ρ, u and p are density, velocity and pressure of the air, respectively. A second order upwind scheme is used to approximate the momentum equation while the pressure–velocity coupling is handled through the SIMPLE method.

2.3. Particle trajectory modelling

A Lagrangian particle tracking method is used to trace the dispersion of particles about their trajectory through integration of the force balance equations on the particle given as

$$\frac{du_p}{dt} = F_D(u_g - u_p) + \frac{g(\rho_p - \rho_g)}{\rho_p} \tag{3}$$

where u_p is the particle velocity and $\rho_p$is the particle density. It is noted that the gravity term (g) was taken as $-9.81\ m/s^2$ in the Y-axis, and hence is applicable for an upright position of the anatomical model. The drag force per unit particle mass is $F_D(u_g - u_p)$ where F_D is given by

$$F_D = \frac{18\mu_g}{\rho_p d_p^2}\frac{C_D \mathrm{Re}_p}{24} \tag{4}$$

where d_p is the particle volume equivalent diameter and μ_g is the molecular viscosity of the fluid.Re_p is the particle Reynolds number, which is defined as

$$\mathrm{Re}_p \equiv \frac{\rho_p d_p |u_p - u_g|}{\mu_g} \tag{5}$$

A low volume fraction of fibres in air is assumed, and therefore the inhaled fibres are primarily influenced by the airflow paths under a one-way coupling approach. Tran-Cong et al. (2004) define the drag force for fibres using spherical aggregate particles clustered into a cylindrical bar configuration. Two equivalent diameters and a shape factor called the "degree of circularity" (Wadell, 1933) are used for this empirically defined drag correlation, which is given as

$$C_D = \frac{24}{\mathrm{Re}_p}\frac{d_A}{d_n}\left[1 + \frac{0.15}{\sqrt{c}}\left(\frac{d_A}{d_n}\mathrm{Re}_p\right)^{0.687}\right] + \frac{0.42(d_A/d_n)^2}{\sqrt{c}[1 + 42500((d_A/d_n)\mathrm{Re}_p)^{-1.16}]} \tag{6}$$

where the volume equivalent sphere diameter (also known as the nominal diameter) is defined as

$$d_n = \sqrt[3]{6V/\pi} \tag{7}$$

where V is the particle volume. The surface equivalent sphere diameter is defined as

$$d_A = \sqrt{4A_{proj}/\pi} \tag{8}$$

where A_{proj} is the projected area of the sphere. The circularity is defined as

$$c = \pi(d_A/P_{proj}) \tag{9}$$

where P_{proj} is the projected perimeter of the particle in its direction of motion. The correlation was implemented into FLUENT via the User-Defined Function allowing a customised drag correlation.

Normalisation of the fibres is performed through Stöber (1972) correlation for an equivalent aerodynamic diameter (d_{ae}) given as

$$d_{ae} = d_{ve}\sqrt{\rho/(1000\kappa)} \tag{10}$$

where d_{ve} is the volume equivalent diameter, ρ is the density of the fibre and κ is the dynamic shape factor for a prolate spheroid. The dynamic shape factor taking the length oriented perpendicular to the flow is given as

$$\kappa_{\perp} = \frac{(8/3)(\beta^2-1)\beta^{1/3}}{(2\beta^2-3)/\sqrt{\beta^2-1}\ln(\beta+\sqrt{\beta^2-1})+\beta} \tag{11}$$

and also for the length oriented parallel to the flow is given as

$$\kappa_{||} = \frac{(4/3)(\beta^2-1)\beta^{1/3}}{(2\beta^2-1)/\sqrt{\beta^2-1}\,\ln(\beta+\sqrt{\beta^2-1})-\beta} \tag{12}$$

where β is the aspect ratio and is defined as the ratio of the fibre length to the diameter.

For random orientation of the fibre, the shape factor is a combination of the two orientations and is given as

$$\frac{1}{\kappa_R} = \frac{1}{3\kappa_{||}} + \frac{2}{3\kappa_{\perp}} \tag{13}$$

Taking the random orientation for the dynamic shape factor, the equivalent aerodynamic diameter range for carbon fibre is 7.6–12.8 μm for lengths of 10–300 μm respectively. For asbestos fibres at the same length range, the d_{ae} range is 1.0–1.6 μm. This is due to the properties of asbestos exhibiting a light density and small cross-sectional diameter causing the d_{ae} to be independent of its length.

Preliminary evaluation of the fibre drag model using a previously constructed nasal-cavity-only model referred to as NC1 (Nasal Cavity 1 in Fig. 2a) is performed. It is noted that the nasal cavity within the integrated respiratory model is extracted out and is referred to as NC2 (Nasal Cavity 2 in Fig. 2b). The deposition efficiency of carbon fibres in NC1 is compared with the experimental data of Su and Cheng (2005) which used carbon fibre, while the other literature data (Cheng et al., 1996; Kelly et al., 2004; Pattle, 1961) used a spherical particle (Fig. 3). The results show a shift in the fibre deposition curve of Su and Cheng (2005) to the right in comparison to the deposition of spherical particles. The fibre drag coefficient model also shows a consistent trend in producing a close match with the experimental fibre deposition data.

2.4. Fibres from carbon and glass composite materials

The diameter of carbon fibres decreases with increasing temperature (above ~500 °C) and duration of fire due to surface oxidation effects. Feih and Mouritz (2012) have measured the reduction in the average diameter of carbon fibres as functions of temperature and heating time using the thermo-gravimetric analysis (TGA), and the results are summarised in Tables 1 and 2. The values presented assume a uniform diameter for all fibres within the smoke plume. However, a limited amount of data in the literature does show that fibre diameter will vary considerably (Mouritz, 2009), presumably due to the turbulent nature of the plume which has different temperatures in different regions.

Furthermore data presented from Gandhi et al. (1999) showed the variation in fibre diameter of carbon fibres before and after a fire (of unknown temperature and time), where a large percentage of fire-affected fibres had diameters between 3 and 4 μm. For glass fibres, the diameter does not change with fire temperature when below the softening temperature of ~1100–1200 °C. The diameter of virgin fibreglass is about 12 μm. The length of the carbon and glass fibres in the smoke plume is random, although there is a lack of published data on the distribution of fibre lengths within a smoke plume. Therefore considering the current published data, a median fibre diameter of 3.7 μm and 12 μm is used for carbon and glass, respectively, and a range of fibre lengths (10, 50, 75, 100, 500 and 1000 μm) is investigated.

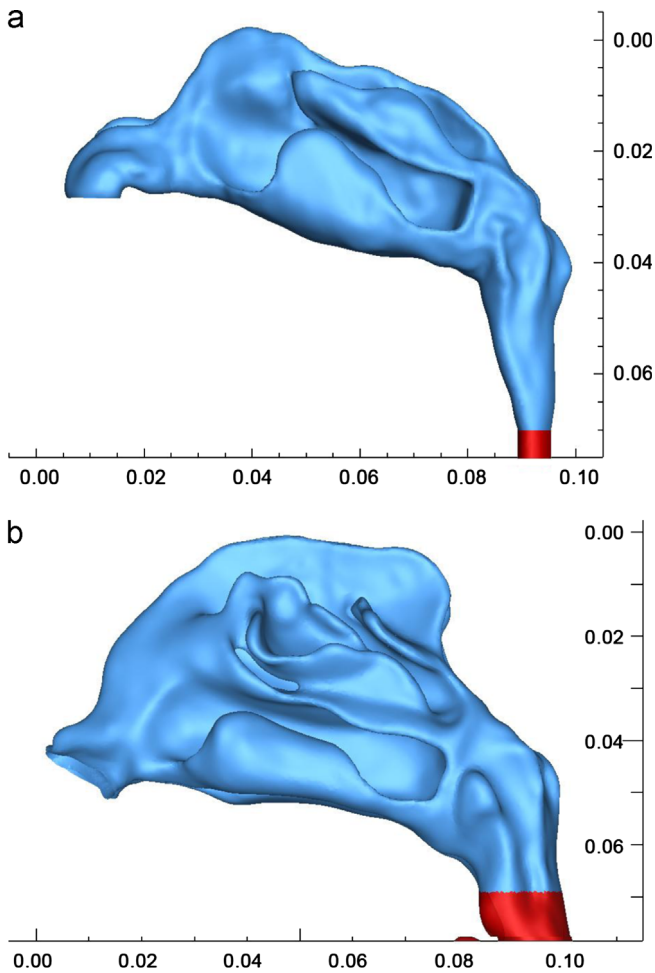

Fig. 2. (a) Nasal Cavity Model 1 (NC1) and (b) Nasal Cavity Model 2 (NC2). Nasal cavity geometry models NC1 and NC2 used for comparisons of fibre deposition.

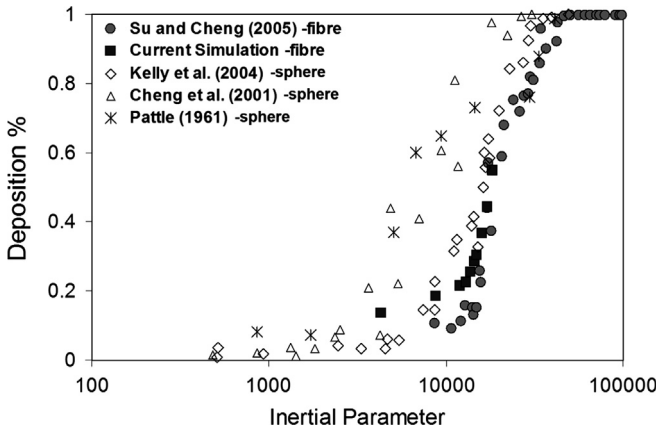

Fig. 3. CFD model results comparison with experimental data that used carbon fibre, and spherical particles.

Table 1
Effect of fire temperature (for a constant heating time of 1 h).

Temperature (°C)	600	650	700	750
Average fibre diameter (μm)	6.5	5.6	4.3	1

Table 2
Effect of fire time (for a constant temperature of 650 °C).

Time (min)	0	15	60	120	180
Average fibre diameter (μm)	7	6.1	5.6	3.5	0.9

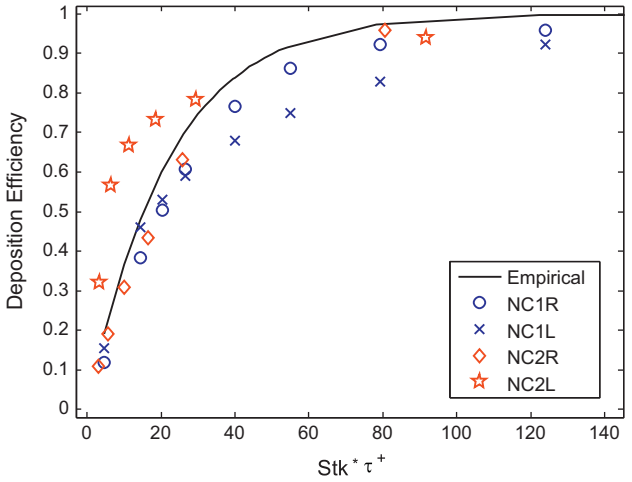

Fig. 4. Predicted fibre deposition for the left and right cavities of NC1 and NC2 compared with an empirical correlation $\tau^{+} = \rho_0 d_a^2 D' \Delta P / \mu^2 L'$ by Wang et al. (2008).

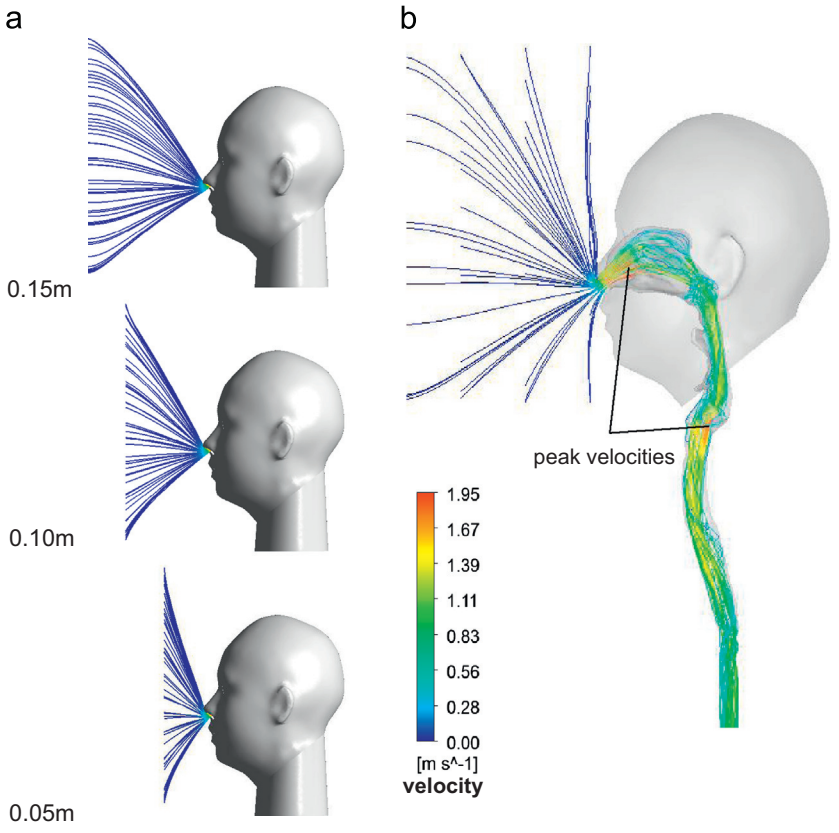

Fig. 5. Airflow streamlines showing inhalation paths from the outside air and into the respiratory airway. Peak velocities are shown in the nasal cavity and laryngeal region. (a) streamline paths released from different upstream locations (b) combined streamline paths passing through the respiratory airway.

3. Results and discussion

3.1. Fibre deposition comparisons

Two nasal cavity models, NC1 and NC2 are used for evaluating the deposition rates for a range of carbon and glass fibre lengths at an inhalation rate of 15LPM. Experimental data from Wang et al. (2008) provide fibre deposition rates in the nasal cavity which is used as comparative data to ensure that the numerical model is valid (Fig. 4). Based on the deposition of glass fibres ($\rho = 2.56$ g/cm^3) of 1 μm diameter Wang et al. (2008) developed an empirical correlation to describe the influences of fibre length, inhalation flowrate, and nasal airway geometry on the deposition efficiency (DE) in a nasal cavity, given as

$$DE = 1 - \exp(aStk\tau^{+}) \tag{14}$$

where a is an empirical constant with value -0.0457, Stk is the particle Stokes number, and τ^{+} is the particle relaxation time defined as

$$\tau^{+} = \frac{\rho_o d_a^2 D_h' \Delta P}{\mu^2 L'} \tag{15}$$

where ρ_o is the density of water, d_a is the aerodynamic equivalent diameter, D_h' is the hydraulic diameter of the nasal valve region, and L' is the axial length from nasal valve to the end of the nasal model.

The CFD predicted results for the deposition efficiency of fibres are given for the left and right cavities, denoted by the letters L and R, of each nasal airway model (NC1 and NC2). The predicted results based on fibre drag in Eq. (6) show good trending comparisons with the empirical correlation by Wang et al. (2008). Low deposition efficiencies are caused by the lower $Stk\tau^{+}$ value while the deposition efficiency rises rapidly with an increase in $Stk\tau^{+}$ before plateauing as it approaches 100% efficiency. $Stk\tau^{+}$ is primarily influenced by the equivalent aerodynamic diameter, d_a, which is strongly influenced by the fibre length, diameter and density, in the form of $\rho A_{cross} L$ were A_{cross} is the cross-sectional area and L is the fibre length (Inthavong et al., 2008). The variation in the predicted deposition efficiency between the different nasal airways is largely influenced by the geometry differences, given that the same modelling procedure is used for each nasal cavity. Figure 3 shows the left cavity of NC2 has much higher deposition than its counterparts, which is due to its more complex curvatures and narrowed passages (Fig. 2) in comparison with NC1L. Despite this, both NC2R and NC1R match well with the empirical data.

3.2. Airflow patterns

Inhalation air streamlines are released from different upstream locations and shown in Fig. 5 to demonstrate the inhalation paths that influence the transport of carbon and glass fibres. A cone-like profile is produced where the air converges from a larger radius in the freestream into the nostrils. The freestream velocity is low while at the nostrils it accelerates rapidly, suggesting that the influence of inhalation is limited to a small region in front of the nose. Figure 6

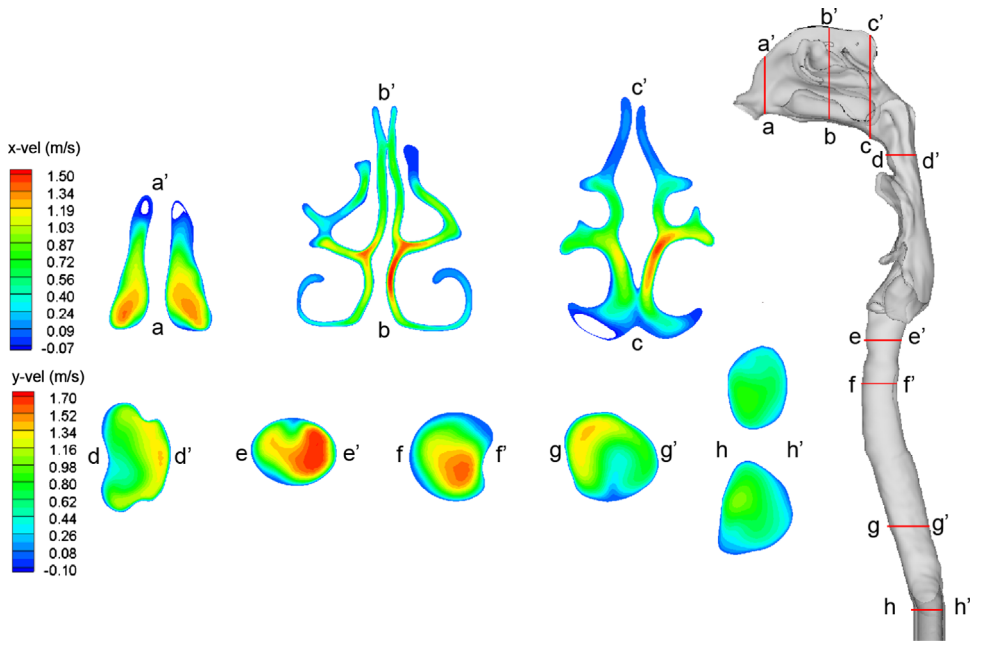

Fig. 6. Axial velocity contours at selected cross-sectional slices.

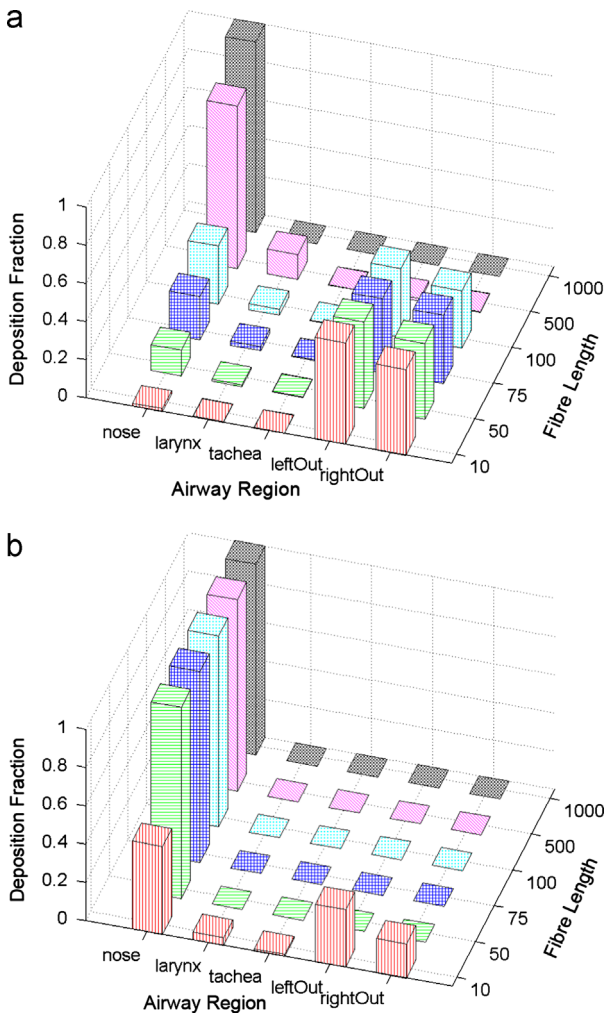

Fig. 7. (a) Local carbon fibre and (b) glass fibre deposition fractions in the respiratory airway. (a) Carbon fibre deposition, $\rho = 1830$ kg/m^3, $\varphi = 3.7$ μm. (a) Glass fibre deposition, $\rho = 2560$ kg/m^3, $\varphi = 12$ μm.

shows axial velocity contours at different cross-sections (in the x- and y-planes) in the respiratory system. The high velocity regions indicate preferential pathways, where the bulk flow is largely found in the middle regions of the nasal cavity and further downstream it is skewed to the rear of the pharyngeal region. Reverse flows are also found in the periphery to some of the cross-section slices.

Inside the respiratory airway, the air flow has an average velocity of 1.3 m/s with peak velocities found at the anterior half of the nasal cavity and at the larynx. The flow patterns provide valuable indicators for potential deposition sites of the inhaled fibres. The fibres are transported by the moving fluid and in the regions of peak velocities, the inertial property of the fibre particle is enhanced. This suggest that fibres exhibiting high inertia (i.e. large values of $\rho A_{cross} L$) will very likely deposit at the peak velocity region. These fibres are also likely to deposit in regions of changing flow directions. This suggests that high deposition may occur in the anterior third of the nasal cavity, and at the posterior nasal airway passage where the flow is changes direction by approximately 90°.

3.3. Local deposition fractions

The deposition fractions of inhaled carbon and glass fibres within different regions of the respiratory airway are shown in Fig. 7. Three deposition regions—nose, larynx and trachea—correspond to the segmented regions highlighted in Fig. 1, while the leftout and rightout regions represent fibres that travel towards the left and right lung, respectively. The results show that the deposition of carbon fibre is sensitive to fibre length; carbon fibre deposition in the lung is prominent for lengths up to 100 μm and longer fibres are deposited mostly in the nasal region. In contrast, deposition of glass fibres in the respiratory airway is independent of length for 50 μm and greater. This is primarily due to the higher density and larger diameter of the glass fibre (12 μm) compared to the carbon fibre (3.7 μm) chosen in this study. The larger density and diameter values

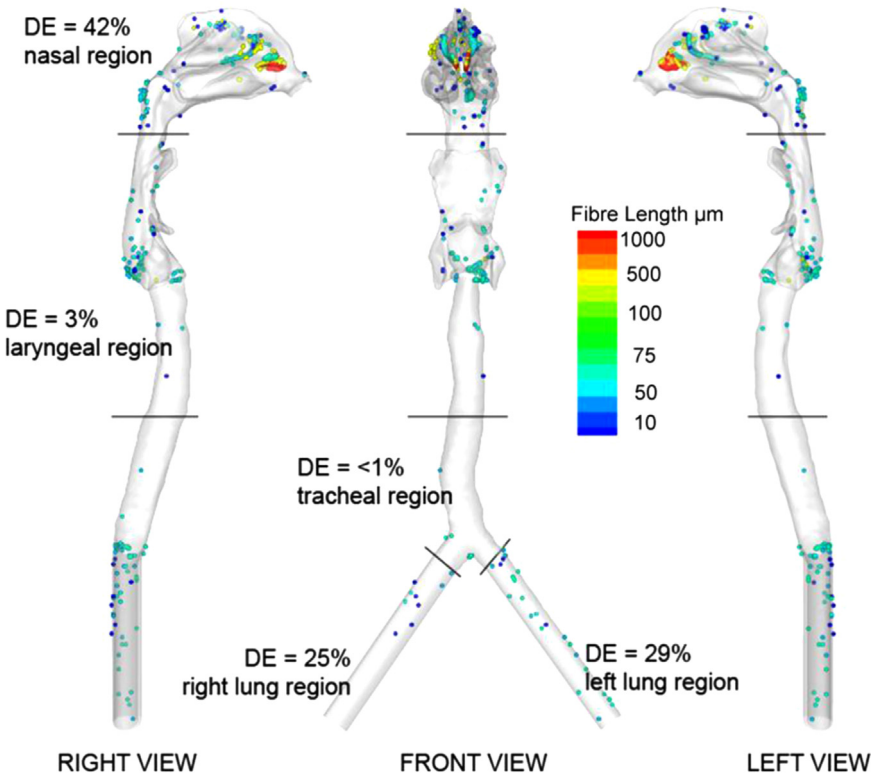

Fig. 8. Regional deposition pattern for carbon fibre at a steady inhalation rate of 15 L/min. Five regions (nasal, laryngeal, tracheal, and right and left lung) and its deposition efficiency (DE) for a uniform concentration over each fibre length is given.

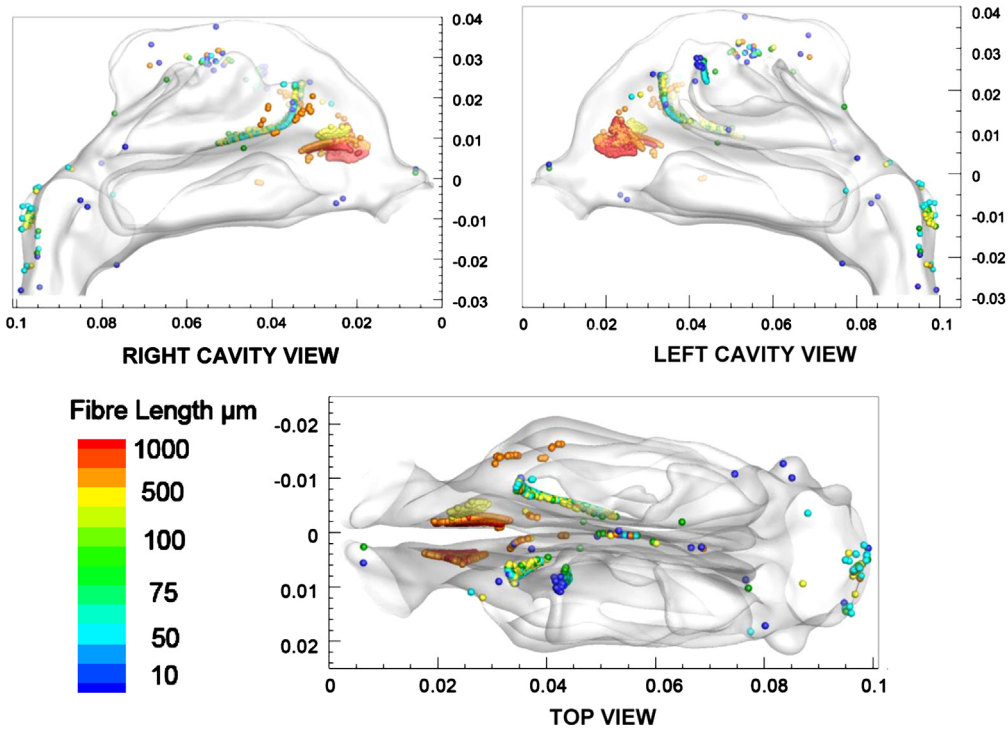

Fig. 9. View of the deposition pattern in the nasal cavity for all fibre lengths of carbon fibre.

increase the glass particle's inertial impactability and therefore enhance its deposition shortly after entering the nasal airway. There is minimal deposition of glass fibres in the laryngeal and tracheal regions, which suggests that glass fibres which pass through the nasal airway have the potential to navigate the remaining convoluted airway passage and into the lung region.

The dependence of deposition fractions on fibre length has important health implications given that fibre toxicity increases with fibre length due to incomplete immune response in the form of released phagocytosis to counter the presence of the foreign particles in the lung airways. Figure 7 shows that lighter density and smaller diameter fibres require much longer lengths for deposition in the nasal cavity, where they may be removed by nose blowing or sneezing. This means that a larger proportion of long fibres, potentially having higher toxic potency, will pass through the nasal cavity and find their way into the lung.

3.4. Carbon fibre deposition patterns

The variation in the deposition pattern for different fibre lengths of carbon fibres is shown in Fig. 8. The DE shown is the averaged value over all fibre lengths that were evaluated. The deposition patterns are coloured by fibre length which shows that a large proportion of nasal deposited fibres are for the longer lengths. In the laryngeal region, deposition is concentrated around the larynx where the airway converges to a narrow passageway before diverging into the curved trachea. Only a small percentage of fibres are found in the tracheal region, since fibres that reach this region have low inertia and therefore are expected to follow the airflow streamlines easily through the trachea. As the airway bifurcates into the left and right main bronchus, the fibres separate with a preference towards the left lung region. This preferential path has been found to the alignment of the left bronchus with the trachea bend of this airway geometry (Inthavong et al., 2010a, 2010b), and its deposition implicates an increase in potential health risks of the left lung. This may also be caused by the airflow distribution in the left and right lung that is different.

The deposition pattern of carbon fibres can be further investigated by analysing in more detail the nasal cavity (Fig. 9). Modelling predicts that a cluster of long fibre lengths are trapped along both nasal septum walls, just after the nostril entrance. The fibres enter the nostrils at an approximate angle of 45° to the horizontal, followed by a sharp change in direction horizontally as the nasal airway widens in the middle region of the cavity. This flow region is characterised with high accelerated flow, as shown in Fig. 5, and this enhances the inertial impactability of the carbon fibres. For smaller fibre lengths, deposition can be found in a more randomly distributed pattern. Further downstream at the posterior region, the flow changes direction once again, and this acts as a further natural physiological defence mechanism by filtering large inertial particles that cannot follow the flow streamlines. This is evident with the longer carbon fibres (100 μm and 500 μm) depositing in this region.

4. Conclusion

An integrated computational model of the respiratory system and surrounding environment was analysed using CFD to simulate the trajectories of carbon and glass fibre fragments from the outside air, through the nostrils and into the respiratory system. The analysis indicates that oxidation-induced thinning of carbon fibres caused by fire increases the likelihood of their deposition within the lung regions when their length is below 100 μm. Longer carbon fibres are trapped within the nose, and therefore are less likely to pose a health risk. Modelling indicates that glass fragments, which are heavier and wider than carbon fibres, are trapped mostly in the nasal cavity since the airway exhibits curvatures, and accelerated flow regions act as a natural filter to high inertial fibre particles. The results in this study show that there are justified concerns regarding the release of fibre fragments (particularly carbon filaments) into the smoke plume of burning composites, such as occurs in a post-crash aircraft accident.

Acknowledgement

The financial support provided by the Australian Research Council (project ID DP120103958) is gratefully acknowledged.

References

Anthony, T.R., & Flynn, M.R. (2006). Computational fluid dynamics investigation of particle inhalability. *Aerosol Science*, *37*(6), 750–765.

Asgharian, B., & Anjilvel, S. (1995). The effect of fiber inertia on its orientation in a shear flow with application to lung dosimetry. *Aerosol Science and Technology*, *23*(3), 282–290.

Cheng, Y.S., Yeh, H.C., Guilmette, R.A., Simpson, S.Q., Cheng, K.H., & Swift, D.L. (1996). Nasal deposition of ultrafine particles in human volunteers and its relationship to airway geometry. *Aerosol Science and Technology*, *25*(3), 274–291.

Feih, S., & Mouritz, A.P. (2012). Tensile properties of carbon fibres and carbon fibre–polymer composites in fire. *Composites Part A: Applied Science and Manufacturing*, *43*(5), 765–772.

Gandhi, S., Lyon, R., & Speitel, L. (1999). Potential health hazards from composites. *Journal of Fire Sciences*, *17*(1), 20–41.

Gradoń, L., & Podgórski, A. (1992). Experimental study on fibrous particle deposition in the human nasal cast. *Journal of Aerosol Science*, *23*(Suppl. 1 (0)), 469–472.

Hesterberg, T.W., Miiller, W.C., McConnell, E.E., Chevalier, J., Hadley, J.G., Bernstein, D.M., Thevenaz, P., & Anderson, R. (1993). Chronic inhalation toxicity of size-separated glass fibers in Fischer 344 rats. *Fundamental and Applied Toxicology*, *20*(4), 464–476.
Inthavong, K., Choi, L.T., Tu, J.Y., Ding, S., & Thien, F. (2010a). Micron particle deposition in a tracheobronchial airway model under different breathing conditions. *Medical Engineering and Physics*, *32*(10), 1198–1212.
Inthavong, K., Ge, Q.J., Li, X., & Tu, J.Y. (2013). Source and trajectories of inhaled particles from a surrounding environment and its deposition in the respiratory airway. *Inhalation Toxicology*, *25*(5), 280–291.
Inthavong, K., Ge, Q.J., Li, X.D., & Tu, J.Y. (2012). Detailed predictions of particle aspiration affected by respiratory inhalation and airflow. *Atmospheric Environment*, *62*(0), 107–117.
Inthavong, K., Tu, J.Y., & Ahmadi, G. (2009). Computational modelling of gas–particle flows with different particle morphology in the human nasal cavity. *Journal of Computational Multiphase Flows*, *1*(1), 57–82.
Inthavong, K., Tu, J.Y., & Heschl, C. (2011). Micron particle deposition in the nasal cavity using the v2-f model. *Computers and Fluids*, *51*(1), 184–188.
Inthavong, K., Tu, J.Y., Ye, Y., Ding, S., Subic, A., & Thien, F. (2010b). Effects of airway obstruction induced by asthma attack on particle deposition. *Journal of Aerosol Science*, *41*(6), 587–601.
Inthavong, K., Wen, J., Tian, Z.F., & Tu, J.Y. (2008). Numerical study of fibre deposition in a human nasal cavity. *Journal of Aerosol Science*, *39*(3), 253–265.
Jeon, K., Yu, I.J., & Ahn, K.-H. (2012). Evaluation of newly developed nose-only inhalation exposure chamber for nanoparticles. *Inhalation Toxicology*, *24*(9), 550–556.
Kelly, J.T., Asgharian, B., Kimbell, J.S., & B.A., W. (2004). Particle deposition in human nasal airway replicas manufactured by different methods. Part 1: Inertial regime particles. *Aerosol Science and Technology*, *38*(11), 1063–1071.
Kennedy, N.J., & Hinds, W.C. (2002). Inhalability of large solid particles. *Journal of Aerosol Science*, *33*, 237–255.
King Se, C.M., Inthavong, K., & Tu, J. (2010). Inhalability of micron particles through the nose and mouth. *Inhalation Toxicology*, *22*(4), 287–300.
Lippman, M. (1990). Effects of fibre charcteristics on lung deposition, retention and disease. *Environmental Health Perspectives*, *88*, 311–317.
Martin, T.R., Meyer, S.W., & Luchtel, D.R. (1989). An evaluation of the toxicity of graphite fiber composites for lung cells in vitro and in vivo. *Environmental Research*, *49*, 246–261.
Mossman, B.T., Lippmann, M., Hesterberg, T.W., Kelsey, K.T., Barchowsky, A., & Bonner, J.C. (2011). Pulmonary endpoints (lung carcinomas and asbestosis) following inhalation exposure to asbestos. *Journal of Toxicology and Environmental Health, Part B*, *14*(1-4), 76–121.
Mouritz, A. (2009). Review of smoke toxicity of fiber-polymer composites used in aircraft. *Journal of Aircraft*, *46*(3), 737–745.
O'Shaughnessy, P.T., Achutan, C., O'Neill, M.E., & Thorne, P.S. (2003). A small whole-body exposure chamber for laboratory use. *Inhalation Toxicology*, *15*(3), 251–263.
Owen, P.E., Glazier, J.R., Ballantyne, B., & Clary, J.J. (1986). Subchronic inhalation toxicology of graphite fibres. *Journal of Occupational Medicine*, *28*, 373–376.
Pattle, R.E. (1961). The retention of gases and particles in the human nose. In C.N. Davies. (Ed.), *Inhaled particles and vapors*. Pergamon Press: Oxford, UK, pp. 302–309.
Shanley, K.T., & Ahmadi, G. (2011). A numerical model for simulating the motions of ellipsoidal fibers suspended in low reynolds number shear flows. *Aerosol Science and Technology*, *45*(7), 838–848.
Stöber, W. (1972). Dynamic shape factors of nonspherical aerosol particles. In T.M. (Ed.), *Assessment of Airborne Particles*. Charles C. Thomas: Springfield, IL, pp. 249–289.
Su, W.C., & Cheng, Y.S. (2005). Deposition of fiber in the human nasal airway. *Aerosol Science and Technology*, *39*, 888–901.
Tannen, K. (1993). Advanced composite materials. *Fire and Arson Investigator*, *1*, 50–51.
Timbrell, V. (1982). Deposition and retention of fibres in the human lung. *Annals of Occupational Hygiene*, *26*, 347–369.
Tran-Cong, S., Gay, M., & Michaelides, E.E. (2004). Drag coefficients of irregularly shaped particles. *Powder Technology*, *139*, 21–32.
Wadell, H. (1933). Sphericity and roundness of rock particles. *Journal Geol*, *41*, 310–331.
Wang, Z., Hopke, P.K., Ahmadi, G., Cheng, Y.-S., & Baron, P.A. (2008). Fibrous particle deposition in human nasal passage: the influence of particle length, flow rate, and geometry of nasal airway. *Journal of Aerosol Science*, *39*(12), 1040–1054.
Whitehead, G.S., Grasman, K.A., & Kimmel, E.C. (2003). Lung function and airway inflammation in rats following exposure to combustion products of carbon-graphite/epoxy composite material: comparison to a rodent model of acute lung injury. *Toxicology*, *183*(1–3), 175–197.